KSCE Journal of Civil Engineering (2019) 23(10):4431-4444

DOI 10.1007/s12205-019-2430-y

Structural Engineering

pISSN 1226-7988, eISSN 1976-3808
www.springer.com/12205

Modeling of Buckling Restrained Braces (BRBs) using Full-Scale Experimental Data

Cigdem Avci-Karatas*, Oguz C. Celik, and S. Ozmen Eruslu*****

Received January 29, 2019/Revised May 28, 2019/Accepted June 19, 2019/Published Online September 3, 2019

Abstract

Hysteretic performance of buckling restrained braces (BRBs) having various core materials, namely, steel and aluminum alloy and with various end connections are numerically investigated. As a computational tool, nonlinear finite element analyses (FEAs) are performed to better model the hysteretic behavior. For the simulation, various aspects such as 1) stress – strain relationship including the strain hardening effect 2) von Mises yield criterion 3) contact surface parameters between the core metal and surrounding high strength grout and 4) friction are defined. Experimental results from near-full scale cyclic tests on two steel core BRBs having steel casing as a restraining environment (named as BRB-SC4 and BRB-SC5) and an aluminum alloy core & aluminum alloy casing tube (named as BRB-AC3) are used in the analyses. All cyclically tested specimens have been designed according to AISC Seismic Provisions. Numerical results obtained from 3D models developed in ANSYS-Workbench give satisfactory response parameters when compared with the experimental ones (e.g., hysteretic curves, dissipated energies). Further, a convergence analysis regarding element numbers in the developed model is conducted for each BRB specimen. Finally, key issues that influence the hysteretic modeling of BRBs are identified.

Keywords: *buckling restrained braces, steel, aluminum alloy, finite element analysis, cyclic loading*

1. Introduction

There are issues associated with true hysteretic modeling and the prediction of Buckling restrained brace (BRB) behavior using numerical methods. These issues include 1) interaction of three materials (core/outer tube, mortar, and unbonding surface), 2) inelastic behavior of the core with various materials and geometrical properties, 3) sliding interface between core and mortar. Reliable and accurate analytical or numerical models considering the above aspects are found to be limited in the literature.

Various models under cyclic loading are available to represent the true BRB behavior in computational modeling studies using numerical analysis. For instance, Sabelli *et al.* (2003) described simplified bilinear elastic-plastic model for BRBs. In a more refined trilinear force-deformation analytical model considering the enhanced BRB strength mainly due to isotropic hardening property is investigated by Fahnestock *et al.* (2007). Other models such as Bouc-Wen smooth law (Black *et al.*, 2004), improved Ramberg-Osgood (providing good approximation for elastic-plastic behavior) law having combined isotropic and kinematic strain hardenings and a model with compression yield load enhanced by 10% (Tremblay *et al.*, 2008) are available in the literature. The Menegotto-Pinto smooth model, again in combination with kinematic and isotropic hardening, has been used to date (Ragni *et al.*, 2011). Similarly, Zona and Dall'Asta (2012) developed both kinematic and isotropic hardening model and the associated parameters that are useful for realistic simulation of the behavior of BRBs that were tested elsewhere. It was found that the model predicted the experimental behavior quite well. It is well known that flexural rigidity of the core section is significantly lesser than the restraining member. The core in general exhibits higher flexural modes mainly resulting from the gap allowed than the buckling restrained mechanism (BRM) as clearly explained by Wu *et al.* (2017). Many researchers followed a half wave length assumption of the core in Euler's Bernoulli theory (Takeuchi *et al.*, 2010; Takeuchi *et al.*, 2012; Takeuchi and Wada, 2017). It was presumed that buckling mode of the core did not affect the restraining force developed by outer restrainer. The fact is that core's buckling wave length is larger than the predicted value by Euler's formula for the case of restrained conditions. Limited analytical studies were reported on the effect of friction on BRBs, while many numerical analyses performed with FE software exist numerical analyses (Hoveidae and Rafezy, 2015; Chou and Chen, 2010; Wang *et al.*, 2012; Tabatabaei *et al.*, 2014). The results of experimental and numerical

*Assistant Professor, Dept. of Transportation Engineering, Yalova University, Yalova 77200, Turkey (Corresponding Author, E-mail: cigdem.karatas@yalova.edu.tr)
**Professor, Structural and Earthquake Engineering Division, Istanbul Technical University, Istanbul 34437, Turkey (E-mail: celikoguz@itu.edu.tr)
***Assistant Professor, Dept. of Mechanical Engineering, Namik Kemal University, Tekirdag 59860, Turkey (E-mail: oeruslu@nku.edu.tr)

studies inferred that the effect of friction is significant on the buckling behavior of BRBs. Chen *et al.* (2016) studied the impact of materials used for the unbonding/sliding surface on BRB response and found that compression strength adjustment factor β is very high for all steel BRBs developed without unbonding materials. Celik and Bruneau (2007) presented a simplified model for bi-directional displacements of ductile end diaphragms of steel girder bridges from unloaded position up to a determined collapse state. It was also mentioned that, inelastic displacement demands in the selected end diaphragm configurations are investigated as they relate to particular design spectrum. The spectral displacement demands are then compared with the target demand of the diaphragms. Celik and Bruneau (2009, 2011) investigated the most efficient geometrical configuration in order to optimize hysteretic energy dissipation through ductile diaphragms having BRBs end diaphragms for the case of straight and skewed steel bridges. Sutcu *et al.* (2014) proposed a simple method for retrofit of existing reinforced concrete (RC) framed buildings to determine the amount of BRBs and steel frame capacity needed.

Based on an overview of previous analytical and numerical works as mentioned above, this paper presents an alternative numerical study using the finite element method (FEM) into hysteretic behavior of BRBs. It has been recognized that limited studies are available to investigate this behavior. In view of this, the present proposes to carry out FE analyses via hysteretic modeling of tested BRBs made up of different core materials and different end connection configurations. For this purpose, a total of 3 BRBs, two having steel core and outer tube, one with aluminum alloy core and outer tube, with similar yield strengths were developed, designed, manufactured, and tested under cyclic loading (Avci-Karatas, 2013; Avci-Karatas *et al.*, 2018). As such, this paper is a numerical expansion of a previously published experimental work of the authors. All the experiments were performed at Structural & Earthquake Engineering Laboratory (STEEL), the Technical University of Istanbul, Turkey. Steel core BRBs use large diameter single bolted (pinned) end connections and rectangular shaped steel core plates as the core materials of S235JR and S355JR. The multi-bolted (weld free) end connections were used in the aluminum alloy BRB having a core material made of A5083-H111. FE analyses are carried out by employing an appropriate cyclic model and the responses are validated against the available experimental results of the specimens. An integrated FE model is proposed to develop by using the commercial FE software, ANSYS-Workbench (2009) for a BRB system considering all geometric and material nonlinearities, inelastic buckling, type of contact, friction, failure phenomenon, and interactions. These details are presented in the subsequent sections. After validation, some parametric studies for various configurations of BRBs are performed to identify the key issues whose influences are determined to be significant on the hysteretic performance of BRBs. Although both experimental and numerical studies on steel core BRBs are available in literature, limited experimental and numerical studies exist on aluminum core BRBs. This study also attempts to compare the experimental and numerical behavior of these two different core BRBs with various end connection details as well. Considering the unbonded surface properties, different core materials, both welded and bolted end connection details, and developing three-dimensional (3D) solid models in CimatronE (2012) and then merging these models into ANSYS-Workbench by minimizing errors and reducing the complexity in modeling are uniqueness of this study.

2. Material Properties

True representation of the material properties is crucial in any numerical modeling. For BRB core materials in this work, a normal yield strength (i.e., S235JR) and a high yield strength (i.e., S355JR) steels and a commercially available aluminum alloy (i.e., A5083-H111 nonheat-treated) rectangular plates are used. Steel tube buckling restrainers (RT-S) use square cross-sections having a steel grade of S355JR. For the aluminum alloy tube (RT-A) used as the buckling restrained environment is made of A6060-T66. Fig. 1 shows the constitutive relations for steel and aluminum core deduced from tensile coupon tests. The abscissa is the engineering strain, ε, and ordinate is engineering strength/stress, σ. Further experimental data of coupon tests are presented in Tables 1 and 2 for steel and aluminum alloy, respectively. These tables describe the values for various parameters to be used in the modeling. In Table 1, ε_0 is equivalent to $0.8\varepsilon_y^{0.2}$ for A5083-H111 as also proposed by Usami *et al.* (2012). 7-day

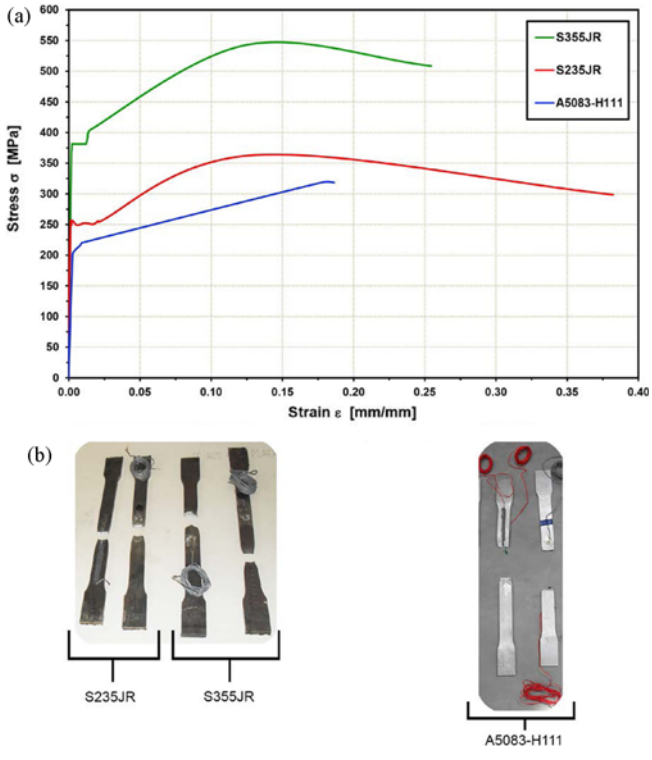

Fig. 1. The Constitutive Relations for Steel and Aluminum Core Deduced from Tensile Coupon Tests: (a) Stress-Strain Curves from the Coupon Tests, (b) Photos from the Coupon Tests

Table 1. Material Properties of Aluminum Alloy Core and Outer Tube

Specimen	Material grade	$\varepsilon_y^{0.2}$ (%)	ε_0 (%)	ε_u (%)	$F_{yc}^{0.2}$ (MPa)	F_{yc}^{0} (MPa)	F_u (MPa)	$\frac{F_u}{F_{yc}^{0.2}}$	E (GPa)
BRB-AC3 (core plate)	A5083-H111	0.27	0.22	20.22	177	141.60	318	1.80	73
RT-A (Outer Tube)	A6060-T66	NA	NA	10	NA	200	227	NA	75

Note: Yield strength of the aluminum alloy BRB core coupons is computed at 0.2% yield strain ($\varepsilon_y^{0.2}$) offset since aluminum alloy did not exhibit definite yield pattern. $F_{yc}^{0.2}$ is the 0.2% yield strength. F_{yc}^{0} is the stress corresponding to the strain ε_0. ε_u = total tensile strain at fracture, F_u = ultimate tensile strength, E = modulus of elasticity.

Table 2. Material Properties of Steel Cores and Outer Tubes

Specimen	Material grade	ε_y (%)	ε_u (%)	F_{yc} (MPa)	F_u (MPa)	$\frac{F_u}{F_{yc}}$	E (GPa)
BRB-SC4 (core plate)	S235JR	0.15	38.21	257	363	1.41	195
BRB-SC5 (core plate)	S355JR	0.19	25.45	373	543	1.46	204
RT-S (Outer Tube)	S355JR	0.38	18.35	345	509	1.48	189

Note: ε_y = yield strain, ε_u = total tensile strain at fracture, F_{yc} = yield strength, F_u = ultimate tensile strength, E = modulus of elasticity.

and 28-day compression strength tests of the non-shrinkage grout gave strengths of 52.3 MPa and 64.1 MPa, respectively. The elastic modulus of the mortar is 37.0 GPa. The other details regarding these specimens are given in Avci-Karatas (2013) and Avci-Karatas *et al.* (2018).

3. Geometric Properties of Modeled BRBs

Figures 2(a) – 2(c) present typical views, plans, and cross section of the specimens employed for modeling for the case of single bolted end connection BRBs and in Fig. 3 for multi-bolted

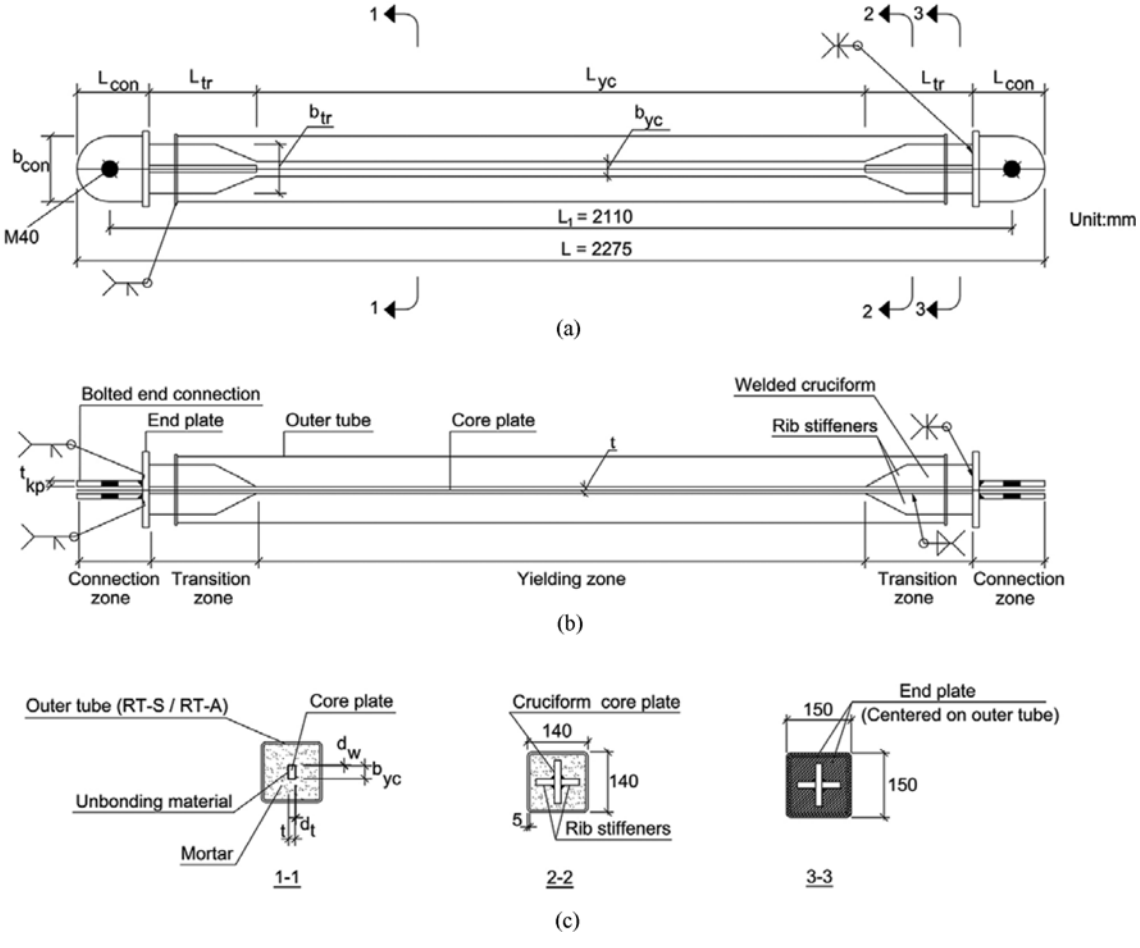

Fig. 2. BRB Configurations for Single Bolted End Connection BRBs (BRB-SC4 and BRB-SC5): (a) Front View, (b) Top View, (c) Cross-sections

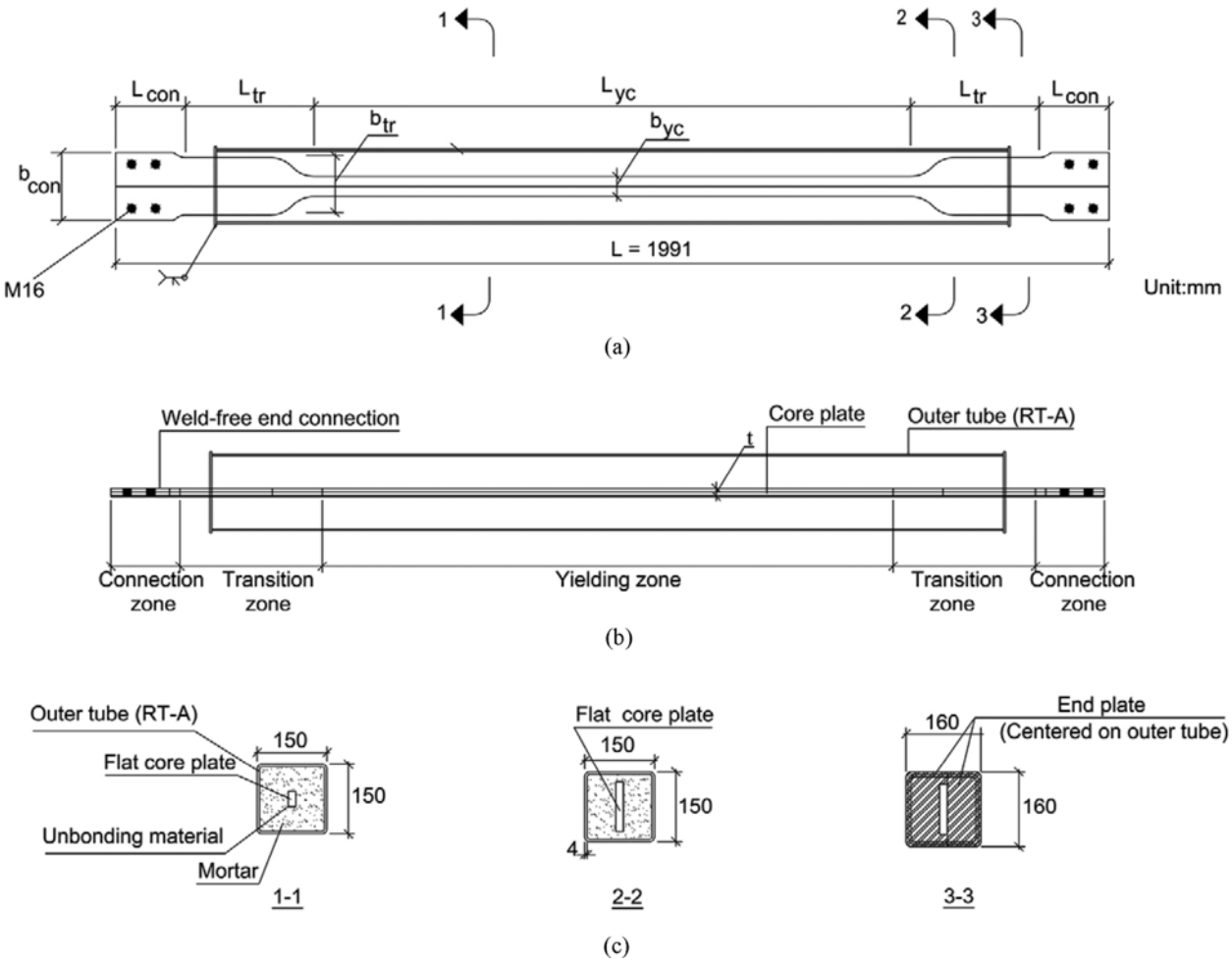

Fig. 3. BRB Configurations for Multi-bolted (Weld-Free) End Connection BRB (BRB-AC3): (a) Front View, (b) Top View, (c) Cross-sections

Table 3. General Geometrical Parameters of the Specimens

Specimen	L_{yc} (mm)	b_{yc} (mm)	t (mm)	L_{con} (mm)	b_{con} (mm)	L_{tr} (mm)	b_{tr} (mm)	L_{yc}/L
BRB-AC3	1,195	40	15	140	137	258	115	0.60
BRB-SC4	1,410	30	16	185	165	249	100	0.67
BRB-SC5	1,380	25	12	184	165	264	98	0.65

Note: The length and width of the yielding portions of the braces are denoted as L_{yc} and b_{yc}. L_{con} and b_{con} are the length and width of the connection portions. The length and width of transition zone are designated as L_{tr} and b_{tr}; where in, t denotes the core thickness.

(weld-free) end connection BRB (BRB-AC3). Table 3 shows the geometrical parameters including the yielding part ratios (60% to 67%). BRBs used a total length of (L) 2,275 mm, a limitation of the testing set-up. The length between work points is 3,339 mm. Pin-to-pin length of BRB-SC4 and BRB-SC5 (L_1) is 2,110 mm. Special unbonding materials were adopted to minimize friction between metal cores and grout.

As per Seismic Provisions for Structural Steel Buildings (AISC 341-10, 2010), core's yield strength, P_{yc}, can be evaluated by following Eq. (1). Note that AISC 341-10 was used here, as this study preceded the publication of the latest AISC document of AISC 341-16.

$$P_{yc} = \beta\omega R_y F_{yc} A_c \quad (1)$$

here, β and ω are compression strength adjustment and strain hardening adjustment factors. Other parameters in this equation are defined in the Notations list. There is no need to apply the factor R_y if P_{yc} can be determined using the yield stress obtained from a coupon material test according to AISC 341-10.

4. Loading Protocol used in Modeling

The test set-up was made of a steel L-frame (a vertical HEA 400 column pinned a steel foundation beam fixed to a concrete strong floor) was designed to accommodate different buckling and non-buckling bracing types and lengths (Haydaroglu and Celik, 2012). Displacement controlled loading protocol was used for all BRB tests. Quasi-static reversed cyclic load was applied

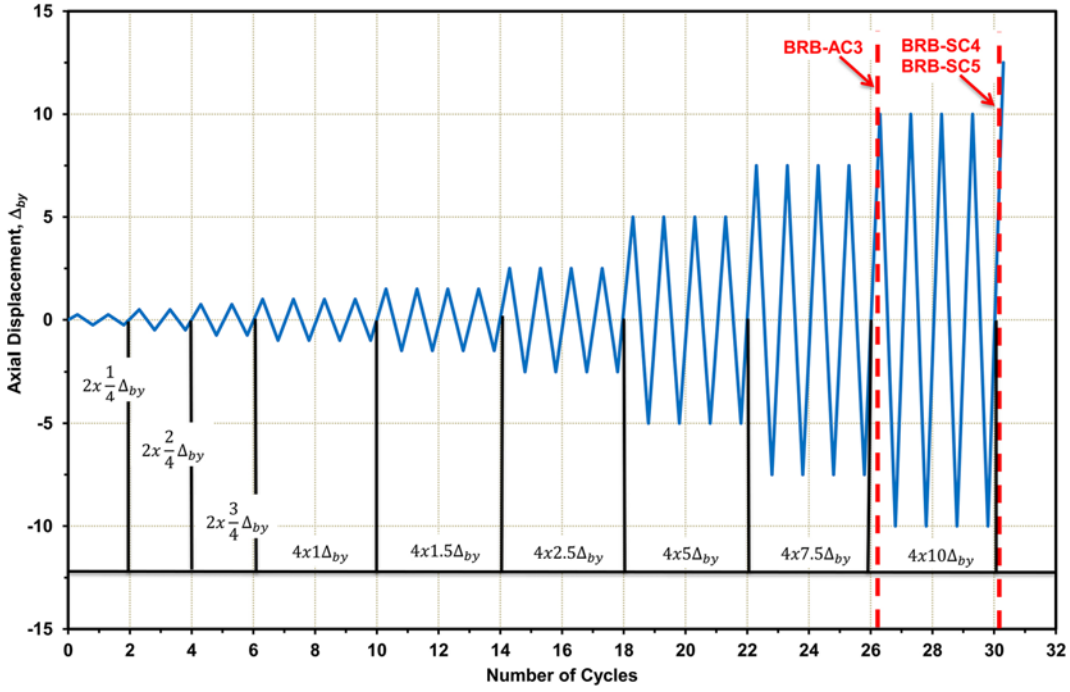

Fig. 4. Loading Protocol

Table 4. Loading Protocol for Elastic and Inelastic Cycles in the Numerical Analyses

Cycle&Axial displacement	BRB-AC3 (mm)	BRB-SC4 (mm)	BRB-SC5 (mm)
$2x1/4\Delta_{by}$	± 1.63	± 1.35	± 1.65
$2x2/4\Delta_{by}$	± 3.26	± 2.71	± 3.29
$2x3/4\Delta_{by}$	± 4.89	± 4.08	± 4.94
$4x1.0\Delta_{by}$	± 6.52	± 5.90	± 6.61
$4x1.5\Delta_{by}$	± 9.78	± 8.85	± 9.92
$4x2.5\Delta_{by}$	± 16.30	± 14.75	± 16.53
$4x5.0\Delta_{by}$	± 32.60	± 29.50	± 33.05
$4x7.5\Delta_{by}$	± 48.90	± 44.25	± 49.58
$4x10\Delta_{by}$	NA	± 59.00	± 66.10

for each BRB as per the guidelines of AISC 341-10. As axial displacements (Δ_{by}) of the braces were dependent on the top lateral displacements of the set-up, these horizontal displacements were considered as the control parameter during the tests. The loading protocol used for the specimens is depicted in Fig. 4. This protocol is also used in the modeling. Table 4 presents sequence of applied loading for elastic and inelastic displacement cycles according to the proposed provision for BRBs. Two gusset plates were modeled as well for proper anchoring to the test set-up. Figs. 5(a), 5(b) and 5(c) show all BRBs before testing. Experimental lateral force-displacement hysteretic and skeleton curves for the tested specimens are also given in the same figure.

5. Hysteretic Modeling

5.1 Parameters and Modeling Assumptions/Simplifications

Numerical models with both geometric and material nonlinearities are developed by using general purpose FE software, ANSYS-Workbench, v.12.0.1 to model the hysteretic behavior of BRBs that were tested earlier by authors under cyclic loads (Avci-Karatas, 2013). 3D solid models are created in CimatronE (2012) which is commonly used CAD/CAM software for manufacturing, tool making, and CNC programming applications, as close to actual test geometry. By this way, BRBs' inner and outer gaps, unbonding mechanism, interaction between the core and the BRM, both bolted (weld-free) and welded end connections, bolt holes, and gusset plates with end/web stiffeners can be taken into count effectively. The created actual size solid models of BRBs are exported from CimatronE to ANSYS-Workbench. Typical general views, lower and upper end views of the created solid models for BRB-AC3, BRB-SC4 and BRB-SC5 are shown in Figs. 6 and 7, respectively.

FEA is a powerful tool to model complex environments and based on the concept of discretization-breaking a model into individual pieces (i.e., meshing). The challenge lies in the development of numerical model is consideration of complexity of the problem in a simplified manner. Note that a simplification without neglecting significant parts that affect the behavior would provide computational time savings as well. In this work, the proposed simplifications as explained in the forthcoming paragraphs have provided the best execution time without any convergence problems that reduce the mesh errors. For example, the plates with welded joints in the end connection zone are merged in CimatronE and considered to be rigid members for FE modeling. On the contrary, high strength mortar as the buckling preventing mechanism (BPM) is included as a whole. Likewise, the gusset plates with rib and edge stiffeners as the bolts and nuts are considered as rigid members. Note that weld zones are not

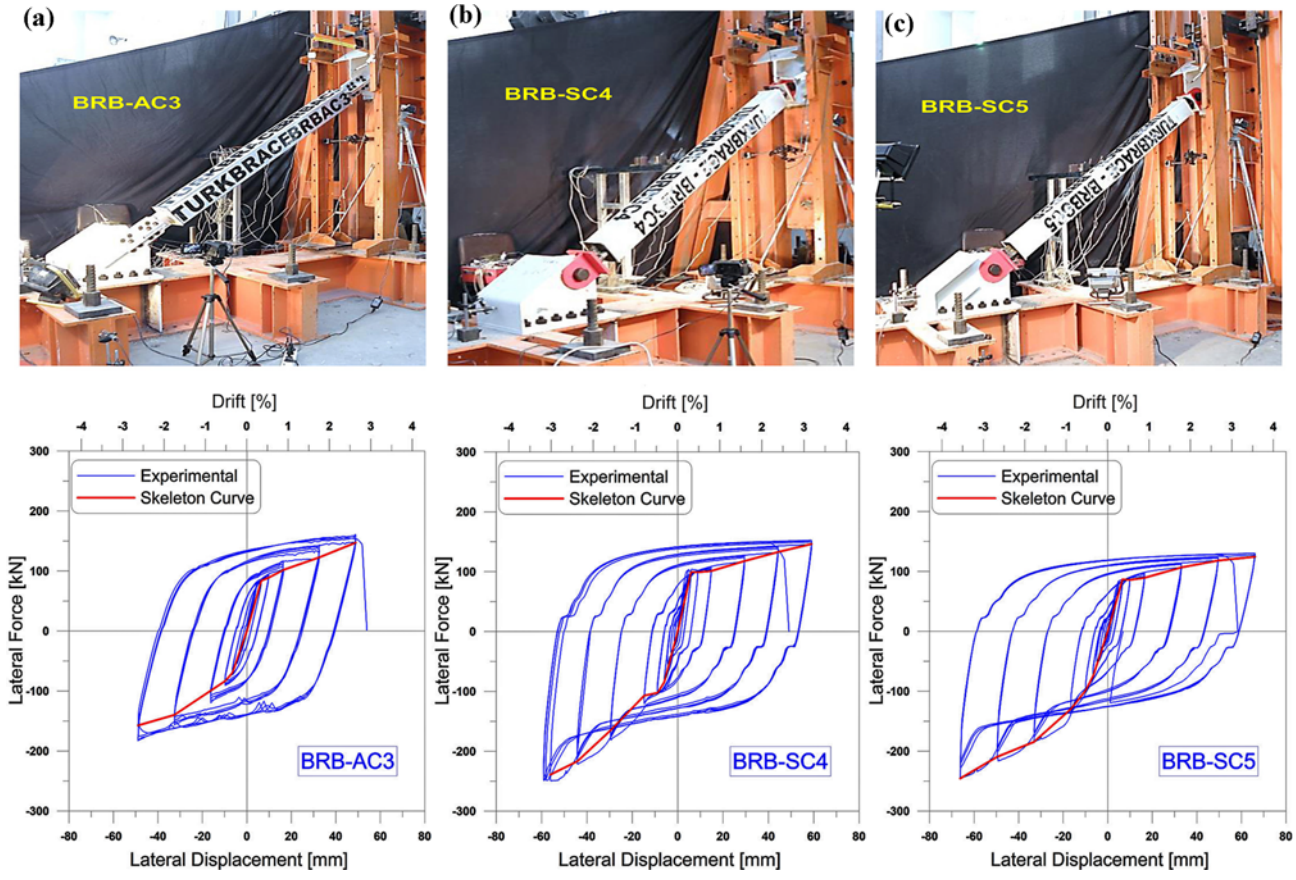

Fig. 5. Overall Views from Specimens Prior to Testing and Experimental Hysteretic Curves with Skeleton Curves: (a) BRB-AC3, (b) BRB-SC4, (c) BRB-SC5 (Note: The upper part shows overall view and the lower part shows its results.)

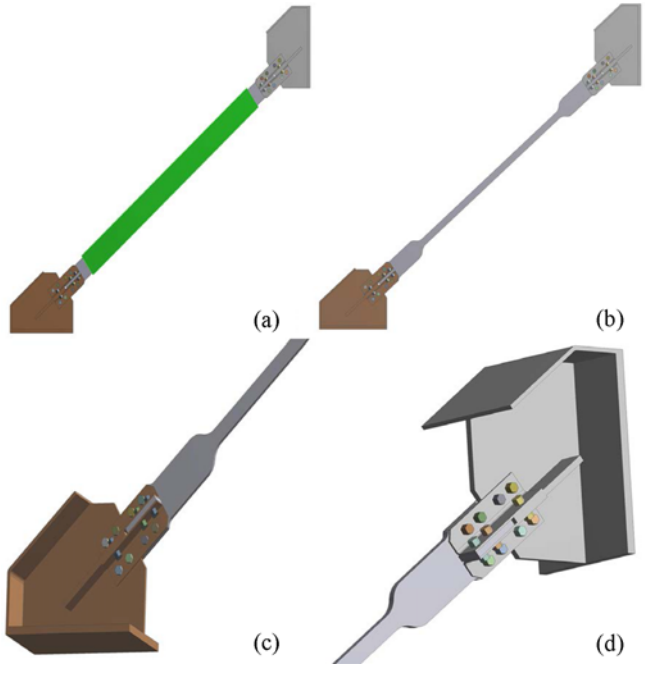

Fig. 6. The Solid Model Details Created for BRB-AC3: (a) General View, (b) View of Core, (c) General View of Lower Connection, (d) View of Upper Connection

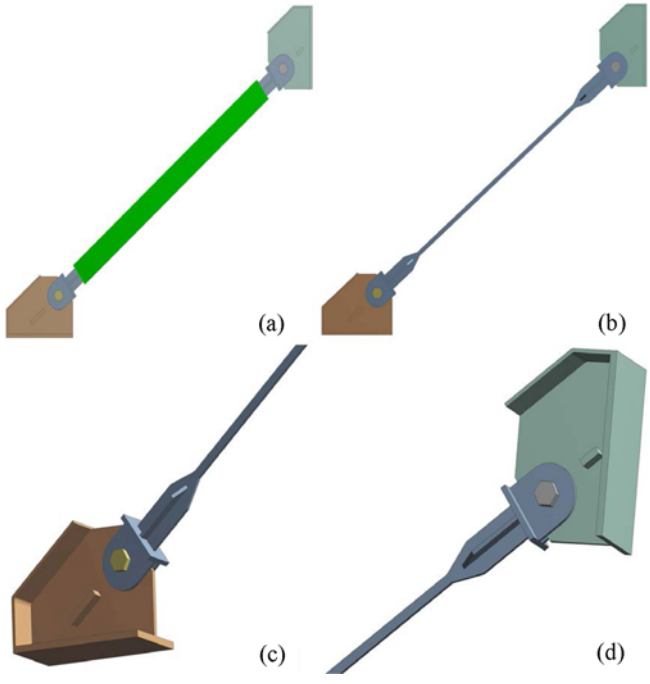

Fig. 7. The Solid Model Details Created for BRB-SC4 and BRB-SC5: (a) General View, (b) View of Core, (c) General View of Lower Connection, (d) View of Upper Connection

modeled since welds designed with high safety factors and elastic behavior is expected. Outer tubes that behave elastically are not modeled in this numerical work to reduce the total degrees of freedom (DOF), decreasing the number of elements especially in contact, and execution time. In BRBs, buckling modes (both global and local in the cores) are prevented by definition. Therefore, axial yielding (both in tension and compression) under cyclic loading is modeled only in the present paper. Also, the outer tube is designed with higher safety factors to prevent buckling.

5.2 Loading and Boundary Conditions

As stated before, the top lateral displacement has been related to the brace axial displacement, which is the reference displacement parameter. Similar to experimental BRB tests as described in Avci-Karatas *et al.* (2018), a displacement-controlled loading protocol given in Fig. 4 is used BRB models in FEA. Contributions of test set-up to the overall hysteretic behavior of BRBs have been eliminated by the acceptance of any eccentricity with the actuator. The horizontal displacement peaks are then applied at the top end of the BRBs. Approximate boundary conditions and constraints are provided in the models. At the lower end, horizontal and vertical displacements of gusset plates are fixed while set free for rotations. On the other hand, horizontal displacement, which allowed axial yielding of the core at the upper end, is taken as free while the displacements of other directions are assumed as fixed and but rotations are released. At the upper and lower surfaces of BRM, displacements and rotations are set to be fixed since no in-plane and/or out-of-plane buckling had occurred during cyclic testing (Takeuchi *et al.*, 2012).

5.3 Meshing

The mesh density is increased by using a finer mesh especially on the yielding portion of the core where large inelastic deformations are expected. This fine meshing enables to sensitively capture the distribution of deformations and von Mises stresses in the yielding zone of the core. These locations might require mesh refinement to obtain a more continuous change in stresses. A coarser mesh is used on the mortar and the gusset plates where an elastic behavior is basically expected. Solid element is best suited to model the phenomenon of global buckling. Three

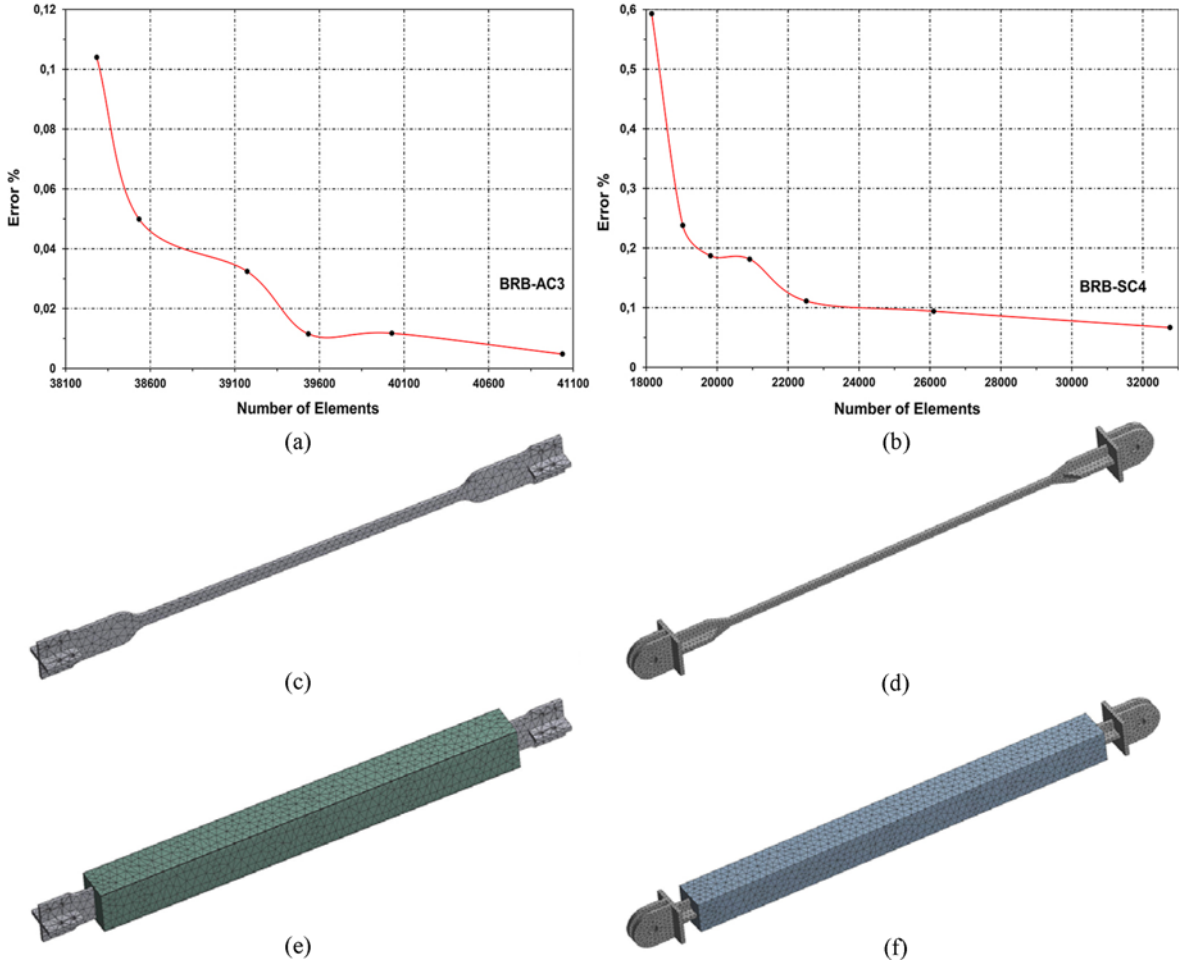

Fig. 8. Convergence Analysis Curves and FE Meshing of BRBs' Core and Mortar: (a) Convergence Analysis Curve of BRB-AC3, (b) Convergence Analysis Curve of BRB-SC4, (c) FE Meshing of BRB-AC3 Core, (d) FE Meshing of BRB-SC4 Core, (e) FE Meshing of BRB-AC3 Mortar, (f) FE Meshing of BRB-SC4 Mortar

dimensional solid elements have been employed to model various BRB components. SOLID45 element is used for meshing of aluminum alloy, steel, and mortar parts in the BRBs. Each element is defined by eight nodes with three DOF at each node, i.e., three translations in three directions. Mesh sensitivity analyses (convergence study) are also performed for BRB-AC3 and BRB-SC4 for one loading cycle to get on idea of the model developed. In these analyses, relationship between the mesh size and the percentage error of the numerical response of the specimens is given for BRB-AC3 and BRB-SC4 as shown in Figs. 8(a) and 8(b), respectively. Thus, the most appropriate meshing is selected and further analyses are executed. In this paper, it is aimed to estimate the minimum structural stress error in FEA. The percentage of structural stress error calculation is found from the von Mises stress variation with number of elements. Flat curves given in the convergence graphs of structural stress error data may be eliminated with frequent intervals mesh sizes. Since a large amount of elements mainly from contact surfaces and increasing number of bolted connections exist in the models, some convergence deviation problems have been encountered and therefore the minimum stress error has been used instead. The mesh sensitivity analysis performed for BRB-AC3 uses six mesh sizes, namely 100 mm (38284 elements), 50 mm (38534 elements), 35 mm (39173 elements), 30 mm (39535 elements), 25 mm (40028 elements), and 20 mm (41037). As seen in Fig. 8(a), the lowest error is related to the model with a mesh size of 30 mm to provide minimum computational time with accurate results for BRB-AC3. To achieve an optimal mesh size for BRB-SC4, seven mesh sizes are tested, namely 75 mm (18154 elements), 35 mm (19030 elements), 30 mm (19813 elements), 25 mm (20919 elements), 20 mm (22513 elements), 17 mm (26106 elements), and 15 mm (32770 elements). As seen in Fig. 8(b), the lowest error is related to the model with a mesh size of 17 mm to provide the minimum computational effort with accurate results for BRB-SC4. The optimal FE mesh is given in Figs. 8(c) and 8(d) for core of BRB-AC3 and BRB-SC4, Figs. 8(e) and 8(f) for mortar of BRB-AC3 and BRB-SC4, respectively. It is shown that the selected mesh sizes are found to be adequate for providing sufficient accuracy with minimum computational time for all BRBs.

5.4 Contact Surfaces

Contact surfaces are also crucial in BRB modeling to define the relationship in the material interfaces for providing load transfer by connecting the FE mesh node points together. In this work, contact surfaces formed by using the contact elements are as follows:

In the numerical model, geometric imperfection between the core and mortar is created similar to experimental studies for initiation of buckling. The gap between the core and mortar is also required for transverse displacement that is expected to initiate different modes. The mentioned gap is in fact acting as the thickness of the undonding layer. This unbonding material has to have an insignificant frictional coefficient so that the core could act independent of the mortar and should exhibit similar tension and compression behaviors. As per the data of manufacturer, tangential Coulomb frictional contact condition is simulated in FE model. Note that the dynamic frictional coefficient values for Teflon bands used in the experimental part of this work varies between $\mu = 0.02 - 0.04$. Contact sliding with frictional coefficient in between the core and mortar is assumed to have an average value of 0.03. Program-controlled amendment of the frictional contact rigidity parameters (e.g., normal penalty stiffness factor, penetration toleration factor) defined throughout the surface of unbonded material is provided in accordance with the loading protocol at every iteration.

Secondly, the bonded contact is defined between the bolts and bolt holes by considering rigidly bonded pair (i.e., continuous load transfer).

5.5 Definition of Inelastic Behavior

It is very well known that the material behaves differently under static and cyclic loading. With the increase of monotonic load, core material hardens similar to isotropic hardening. In the case of kinematic hardening, material undergoes inelastic strains, the yield surface translates with each load cycle. In case of reversed cyclic loading, combined hardening develops and grows in size. The Bauschinger effect may have a significant influence with regard to the core material grade and hence cannot be ignored for reversed loads (AlHamaydeh *et al.*, 2016; Atasever *et al.*, 2018). For representation of realistic behavior of BRB, combined isotropic and kinematic hardening models are employed in FE modeling.

To this end, multilinear isotropic hardening is employed to model the elastic-plastic behavior of cores in FE modeling. The available experimental data (Avci-Karatas, 2013; Avci-Karatas *et al.*, 2018) are utilized to confirm theoretical estimations on the inelastic behavior of the braces by considering kinematic hardening properties. All material properties gained from the experiments, have been transferred into ANSYS-Workbench FE software. The material properties include mechanical properties of the core material, mortar compressive strength, etc. Combined stress-strain curves of multilinear isotropic material behavior for BRB cores were specified by using both coupon tests assigned to pre-yield and true stress-strain relationship based on the cyclic experimental data assigned to post-yield behavior. Elastic behaviors of mortar and gusset plates are then defined by mortar compressive strength and steel material strength, respectively. Large inelastic deformations develop in BRB cores and these deformations are predominant due to micro-structure dislocation interactions and movements, and require additional energy for subsequent dislocations. To model this post-yield behavior, as mentioned earlier, large inelastic strains from typical 'engineering stress-strain' relationship are converted into 'true stress-strain' based on the experimental data. Consequently, since the steel cores have relatively higher hardening properties than aluminum alloy cores, to achieve faster convergence with inputting true stress-strain values of each core materials, the implicit Hollomon

(1945) model is employed in the present study. Note that fracture is not modeled in this work.

5.6 Strain Hardening and True Stress-Strain Curves

In predicting the strain-hardening behavior of aluminum alloy and steel BRBs using the Hollomon model, stress-strain data of material tests are utilized to obtain the engineering stress-strain values. This issue is also helpful in solving convergence problems. It is assumed that strain hardening primarily begins after yield point of the metal and ends before ductile fracture. Therefore, stress-strain values from the yield (F_{yc}) point up to the ultimate tensile stress (F_u) are considered. A true stress-strain curve ($\sigma_T - \varepsilon_T$) is expressed by the empirical Hollomon's equation as follows:

$$\sigma_T = K\varepsilon_T^n \tag{2}$$

Where, K = strength coefficient
n = strain hardening exponent
ε_T = true strain
σ_T = true stress

For most metals, the strain hardening exponent falls between 01 – 0.5, however, perfectly elastic-plastic solids have strain hardening exponent of zero. By using logarithmic function, this exponential function is mapped onto a straight line ($\log\sigma_T = \log K + n\log\varepsilon_T$), where in slope is equal to the strain hardening exponent (n), and intercept with a true strain value of 1 is the strength coefficient (K). In the coupon tests, ε_T true strain at F_u ultimate tensile stress (engineering stress) is numerically equal to n (i.e., $\varepsilon_T = n$) (Beddoes and Bibby, 1999). Hence, n represents the limiting strain for homogeneous deformation.

Table 5 shows a comparison of the experimental and calculated strain-hardening behaviors for the aluminum alloy and steel BRBs using the Hollomon's model (Hollomon, 1945). ε_T, σ_T and K values of the specimens are calculated and tabulated after the experimental testing. Here, e refers to the base of natural logarithm. A_c and A_k are the cross-sectional areas of the cores before and after testing, respectively. σ^E_{E-BRB} values for the BRBs were calculated by the experimentally obtained maximum and absolute values of axial forces at last excursion (i.e., $F^E_{max-BRB}$ divided by A_c) (Avci-Karatas *et al.*, 2018). Based on the principle of constancy of volumes ($V = A_cL_{yc} = A_kL_k$), the relation between ($\sigma^E_{E-BRB} - \varepsilon_E$) and ($\sigma_T - \varepsilon_T$) of BRBs can be obtained as follows:

$$\varepsilon_T = \ln(\varepsilon_E + 1) \tag{3}$$

$$\sigma_T = \sigma^E_{E-BRB}(\varepsilon_E + 1) \tag{4}$$

As seen in Table 5, the high stress value increase required to have the dislocations continue their movements explains the high true stress values of steel BRBs, which have considerably high hardening as expected. It is known that with increasing flow stress, the strain can be evenly distributed during deformation which leads to improved formability. Therefore, it can be seen that the steel cores would possess better forming abilities compared to the aluminum alloy core. However, even though it is generally recognized that the formability increases with strain hardening exponent, BRB-AC3 core material has exhibited similar behavior since this BRB has yield strength similar to BRB-SC4 (Fig. 1).

6. Results of the Analyses

In this section, the main hysteretic curve analogy relations are characterized via the model presented by Black *et al.* (2004). Other parametric studies resulted in that a simple bilinear model could satisfactorily represent the nonlinear post-yielding behavior of BRBs for structural design purposes (Black *et al.*, 2004). To deduce a relation between maximum brace displacement and yield displacement, a simplified bilinear force-displacement relationship can be used as given in Fig. 9 which also shows the general shape of the main hysteretic curve for maximum force-displacement. With reference to Fig. 9, the maximum force (F_{max}) can be expressed as a function of maximum displacement (u_{max}) and yield displacement (u_y) or an equivalent elastic displacement as follows:

$$F_{max} = K_0u_y + K_1(u_{max} - u_y) \tag{5}$$

$$F_{max} = K_0(u_y + \Delta u_y) \tag{6}$$

where K_0 and K_1 are the initial (elastic/pre-yield) and secondary (tangent/post-yield) stiffnesses, respectively. Here, Δu_y is the change of yield displacement. By equating Eqs. (5) and (6), Δu_y can be obtained as follow:

$$\Delta u_y = \frac{K_1}{K_0}(u_{max} - u_y) = \alpha(u_{max} - u_y) \tag{7}$$

where, α is the ratio of post-yield to pre-yield stiffness. All parameters of model are shown graphically in Fig. 9. F_y and $F_{\Delta u_y}$ are introduced as the yield force corresponding to u_y and the change of force corresponding to Δu_y. In the proposed hysteretic model, expressed by Eqs. (5), (6) and (7), the parameters α, K_0 and K_1 are to be uniquely determined from the experimental results.

Table 5. ε_T True Strain, σ_T True Stress Values and K Strength Coefficients of Specimens

Specimen	$A_c = b_{yc}t$ (mm^2)	$A_k = \frac{A_cL_{yc}}{L_k}$ (mm^2)	$F^E_{max-BRB}$ (kN)	σ^E_{E-BRB} (MPa)	$\varepsilon_E = \frac{A_c - A_k}{A_k}$ (%)	$\varepsilon_T = n$ (%)	σ_T (MPa)	$K = \sigma^E_{E-BRB}\left(\frac{e}{n}\right)^n$ (MPa)
BRB-AC3	600	502.52	219.14	365.23	19.40	17.73	436.19	592.61
BRB-SC4	480	410.96	294.28	613.08	16.80	15.53	716.08	956.25
BRB-SC5	300	265.28	281.78	939.27	13.09	12.30	1,062.22	1,374.51

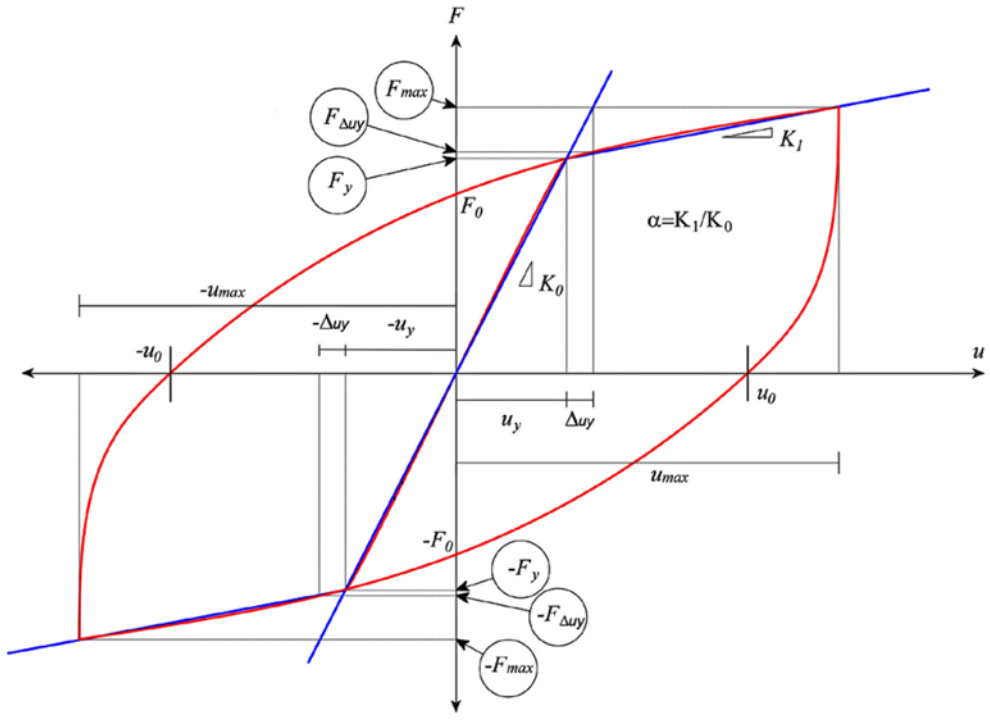

Fig. 9. General View of the Main Hysteretic Curve for Analytical Modeling

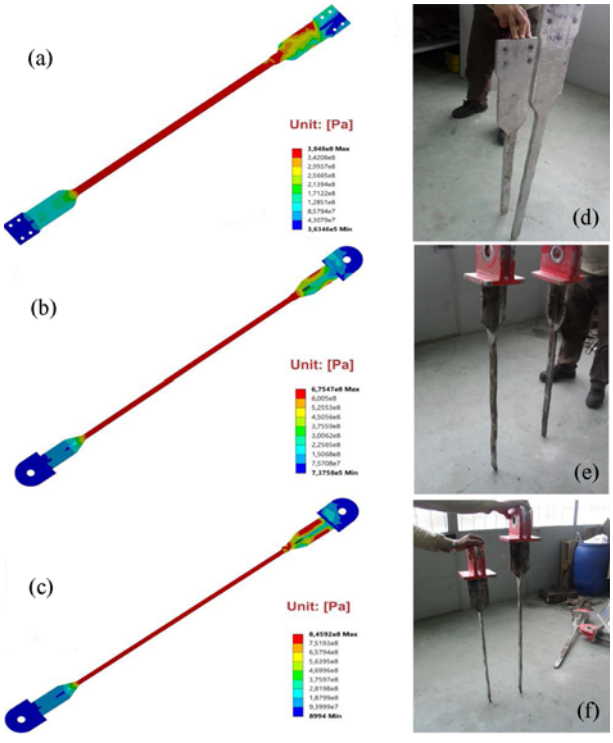

Fig. 10. Numerical versus Experimental Behavior at Last Cycle: (a) Von Mises Stress Distributions in BRB-AC3, (b) Von Mises Stress Distributions in BRB-SC4, (c) Von Mises Stress Distributions in BRB-SC5, (d) Core Fracture in BRB-AC3, (e) Core Fracture in BRB-SC4, (f) Core Fracture in BRB-SC5

Based on the modeling assumptions as explained in the previous sections, Figs. 10(a), 10(b) and 10(c) presents the resulting von Mises stress distributions on the core at the last cycle of FEA for the specimens. Although fracture is not simulated in the present studies, the overall behavior is well captured until fracture and experimental rupture occurred at a point close to the mid-point of the yielding zone as designed and expected in all BRBs (Figs. 10(d), 10(e) and 10(f)). Note that these obtained maximum von Mises stresses are a bit (max. %20.3 for BRB-SC5) different from the values presented in Table 5 (σ_T), mainly due to simplified assumptions made in the computation of the axial loads and stresses, boundary conditions, and combined effects (i.e., axial load and local bending) in the core member. In the upper end transition zone of BRBs, some limited areas are excessively stressed mainly from the hinged joints that behave non-ideally (i.e., semi-rigidity). These stresses are caused by local in-plane or out-of-plane bending moments due to the existing bending stiffness of the connection. The steps followed are diagrammed in Fig. 11 to summarize the process required by the integrated requirements of nonlinear FE hysteretic modeling developed herein for the tested BRBs.

7. Comparison of Numerical and Experimental Hysteretic Curves

Stable hysteretic behaviors are obtained for all three BRBs investigated herein. In the FEM modeling, failure behavior of the material is represented through von Mises yield principle considering the strain hardening effects. In FEA analysis, elastic-plastic behavior of metals including hardening effects is

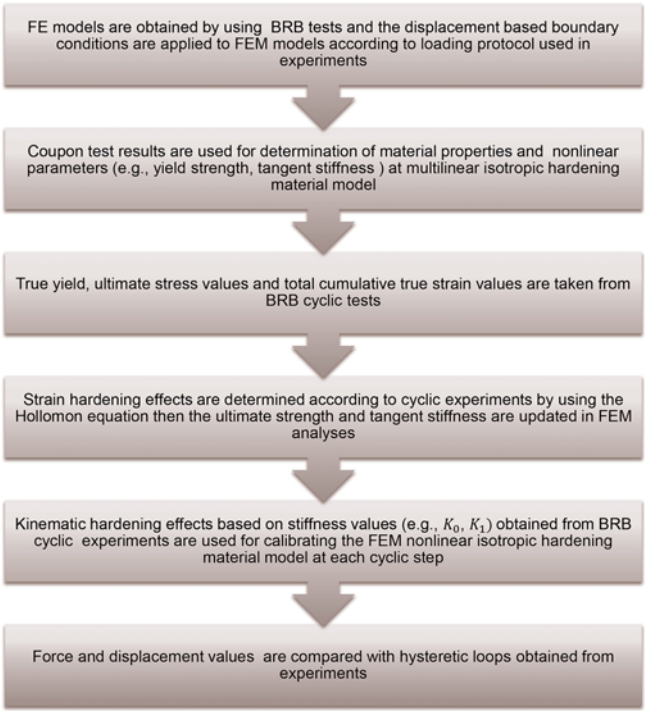

Fig. 11. Flowchart for Hysteretic Modeling of BRBs

generally modeled with bilinear isotropic hardening and bilinear kinematic hardening rules. These models are generally coupled with von Mises yield criteria when work hardening assumptions are made. Close agreement between FE results and the corresponding experimental findings are observed for the developed models. Fig. 12 reveals that, based on the procedure given in this work, hysteretic behavior of BRBs with various properties can be numerically well captured by using experimental data. Because strain hardening properties of aluminum alloy BRB is low, convergence of the numerical results to the experimental ones occurred more rapidly compared to the steel BRBs. This is believed to be an important outcome of this numerical work. As such, more similar and symmetrical results are obtained both in the tension and compression cycles of the aluminum alloy BRB. From the compression peaks in the steel BRBs, it can be noted that sharp ends are formed from both potential increase in the friction between the core and the mortar material and possible manufacturing problems in the inner gap zone. In the modeling, this type of compression hardening behavior is found in other developed BRBs in the literature (e.g., Berman and Bruneau, 2009; Merritt *et al.*, 2003). It is also observed that post-yield experimental and analytical hysteretic curve proximity of the specimens is higher compared to pre-yield displacement

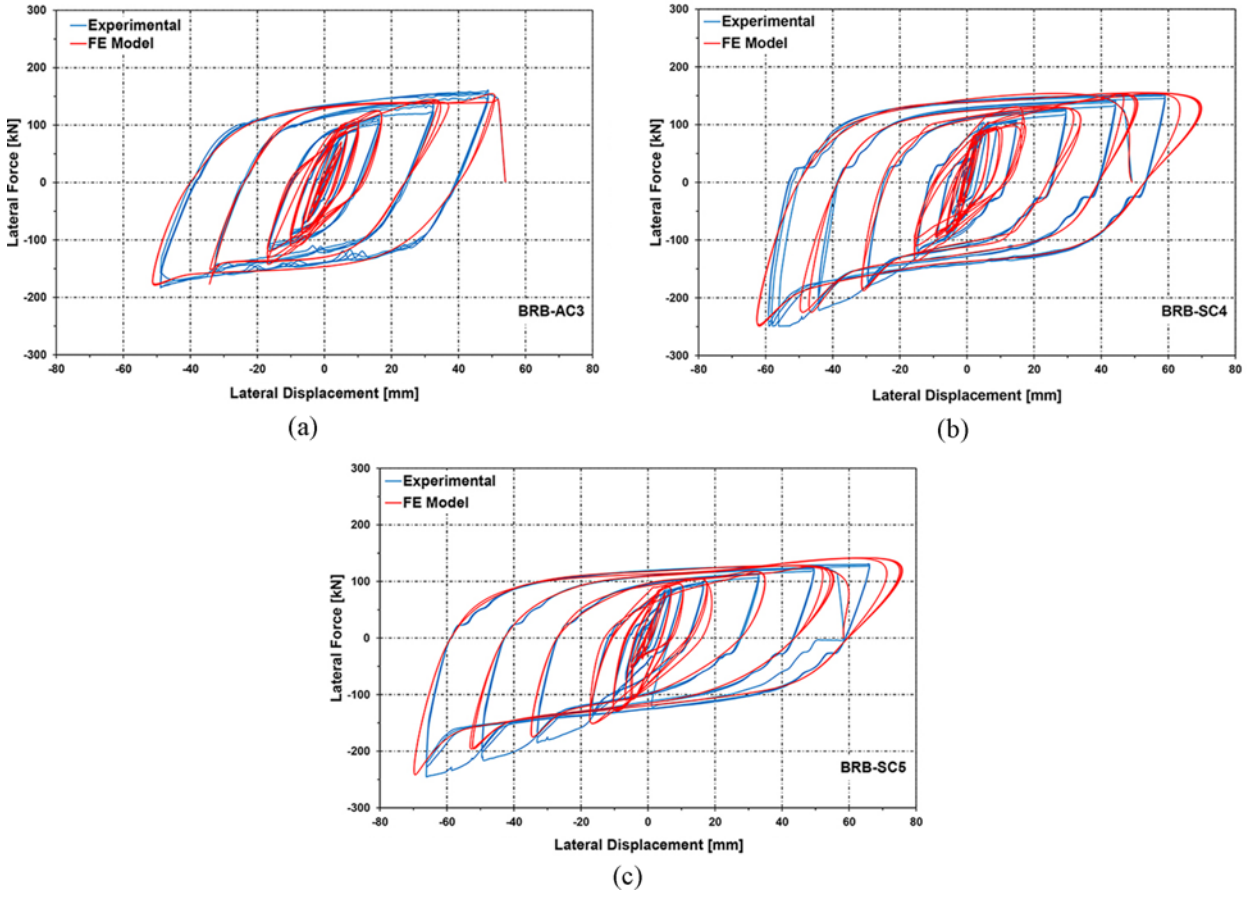

Fig. 12. Comparison of Experimental and FE Results: (a) BRB-AC3, (b) BRB-SC4, (c) BRB-SC5

Table 6. Comparison between Experimental and Analytical Results

Specimen	Cycle	Drift (%)	E_h^E (kN.mm)	E_h^A (kN.mm)	T_{max}^E (kN)	P_{max}^E (kN)	T_{max}^A (kN)	P_{max}^A (kN)	$\frac{T_{max}^E}{T_{max}^A}$	$\frac{P_{max}^E}{P_{max}^A}$
BRB-AC3	26	2.63	137,301.40	142,305.10	153.25	-174.00	150.11	-174.67	1.02	0.99
BRB-SC4	30	3.17	248,507.90	240,374.60	149.63	-247.38	145.50	-238.60	1.03	1.04
BRB-SC5	30	3.55	247,763.50	240,310.90	127.50	-225.00	134.55	-240.13	0.95	0.94

steps.

Seismic efficiency of BRBs system can generally be measured in terms of cumulative energy dissipation by calculating the total area under hysteretic curves. The comparison of experimental and numerical E_h values for the last cycle and drift of each specimen and experimental/numerical ratios of the tension and compression force peaks (T_{max} and P_{max}) of that cycle are summarized in Table 6. The exponent E and A indicate the experimental and numerical values, respectively. Stiffness of the BRBs in both experimental and FEA in the different cycles are very close to each other and almost equal since the loops are very close to each other. It is shown that resistance of the braces is not much different on the tension side.

8. Conclusions

An efficient numerical simulation has been performed to capture the true hysteretic behavior of BRBs consisting of different core materials and end connections. A total of 3 energy dissipative BRBs, 2 with steel core (S235JR and S355JR) and outer tube, 1 with aluminum alloy core (A5083-H111) and aluminum outer tube, with similar yield strengths are developed, designed, manufactured, and cyclically tested as per AISC 341-10. Numerically obtained hysteretic curves, response parameters are predicted and compared with the corresponding experimental observations. The existing experimental data of authors are used to model the behavior of BRBs. Based on the numerical findings, the following main observations and conclusions can be deduced:

1. Verification of the experimental hysteretic behaviors of BRBs (steel and aluminum alloy) was performed by a 3D modeling under reversed cyclic loadings. ANSYS-Workbench program was used effectively in order to examine the nonlinear material and geometric properties of the specimens. All solid models were created by using CimatronE and exported to ANSYS-Workbench.
2. Hardening differences in aluminum alloy and steel BRB specimens were reflected in the analyses by using the strain hardening exponent which was found to be a powerful tool for this purpose. Fractured core cross-sectional areas of the specimens after testing were determined by cutting the specimens in half after each testing. By this way, the true stress values obtained from the fractured cores made it possible to be used in the analyses.
3. It is illustrated that hysteretic behavior of all BRBs investigated in this work can be well numerically captured by using the full experimental data. All three BRBs fractured in the middle section of the yielding zone as designed. This inelastic behavior is also observed in the modeled BRBs.
4. Connection parts are needed to be modeled to take into account their contribution to axial deformation in the elastic stage. The connection members are modeled as rigid members to simplify the problem. Also, experimental results show that this assumption is quite reasonable since axial displacements are sufficiently estimated and no significant slippage has been observed in the hystereses.
5. Due to relatively lower strain hardening in the aluminum alloy BRB, convergence has occurred more rapidly compared to the steel BRBs in which higher strain hardening behavior has been observed.
6. The computed experimental/numerical ratios of the maximum tension and compression force values of T_{max}^E/T_{max}^A and P_{max}^E/P_{max}^A were found to be between 0.95 – 1.02 and 0.94 – 1.04, respectively.
7. Note that, to follow the procedure given here, complete experimental data are required for a better modeling. This is why the proposed model has been applied only on the authors' available test data. However, the model could be applied for other test results by others when all data are available (from coupon tests to full-scale BRB testing data).

In summary, the hysteretic behavior of BRBs has been numerically simulated by using ANSYS-Workbench and found that a good agreement between predicted and experimental responses. Hence, the proposed model is robust and reliable; the same road map can be used in modeling of BRBs when full-scale cyclic test results are available.

Acknowledgements

The authors acknowledge the supports by the Scientific and Technological Research Council of Turkey (TUBITAK, Project No: 110M776) and the Istanbul Technical University Research Projects Unit (ITU-BAP, Project No: 33459).

Notations

A_c = Area of the core
A_k = Area of the core after testing
b_{con} = Connection parts' width of brace
b_{tr} = Width of the transition zone of the brace
b_{yc} = Yielding parts' width of brace
E = Young's modulus

F_y = Yield force corresponding to u_y
F_{yc} = Specified minimum yield stress
$F_{yc}^{0.2}$ = 0.2% yield strength/stress
F_{max} = Maximum force
F_u = Ultimate tensile strength/stress
$F_{\Delta uy}$ = Change of the force corresponding to Δu_y
K = Strength coefficient
K_0 = Initial/elastic/pre-yield stiffness
K_1 = Secondary/Tangent/post-yield stiffness
L = Total length of the brace
L_1 = Pin-to-pin length of single bolted end connection brace
L_{con} = Connection parts' length of brace
L_{tr} = Transition parts' length of brace
L_{yc} = Yielding parts' length of brace
n = Strain hardening exponent
P_{max} = Maximum compression force
P_{yc} = Core yield strength
R_y = Expected to specified minimum yield stress ratio
T_{max} = Maximum tension force
u_{max} = Maximum brace displacement
u_y = Yield displacement
α = Post-to pre-yield stiffness
β = Adjustment factor for compression strength
Δu_y = Change of yield displacement
ε = Engineering strain
ε_E = Engineering strain of brace obtained from after testing data
ε_T = True strain
ε_y = Yield strain
$\varepsilon_y^{0.2}$ = 0.2% yield strain
ε_u = Total tensile strain at fracture
μ = Dynamic frictional coefficient
σ = Engineering strength/stress
σ_{E-BRB}^{E} = Experimentally obtained maximum and absolute values of axial forces at last excursion
σ_T = True stress
ω = Strain-hardening adjustment factor

ORCID

Cigdem Avci-Karatas https://orcid.org/0000-0002-6383-1376
Oguz C. Celik https://orcid.org/0000-0001-9448-2562
S. Ozmen Eruslu https://orcid.org/0000-0003-2942-378X

References

AISC 341-10 (2010). *Seismic provisions for structural steel buildings*, ANSI/AISC 341-10, American Institute of Steel Construction, Inc., Chicago, IL.

ANSYS-Workbench (2009). *Products release 12.0.1*, ANSYS, Inc., Canonsburg, PA, USA.

AlHamaydeh, M., Abed, F., and Mustapha, A. (2016). "Key parameters influencing performance and failure modes for BRBs using nonlinear FEA." *J. Constr. Steel Res.*, Vol. 116, pp. 1-18, DOI: 10.1016/j.jcsr.2015.08.038.

Atasever, K., Celik, O. C., and Yuksel, E. (2018). "Development and cyclic behavior of U-shaped steel dampers with perforated and nonparallel arm configurations." *Int. J. Steel Struct.*, Vol. 18, No. 5, pp. 1741-1753, DOI: 10.1007/s13296-018-0074-2.

Avci-Karatas, C. (2013). *Design, fabrication, and cyclic behavior of steel and aluminum alloy core buckling restrained braces (BRBs)*, PhD Dissertation, Istanbul Technical University (ITU), Istanbul, Turkey (in Turkish).

Avci-Karatas, C., Celik, O. C., and Yalcin, C. (2018). "Experimental investigation of aluminum alloy and steel core buckling restrained braces (BRBs)." *Int. J. Steel Struct.*, Vol. 18, No. 2, pp. 650-673, DOI: 10.1007/s13296-018-0025-y.

Beddoes, J. and Bibby, M. (1999). *Principles of metal manufacturing processes*, Elsevier Butterworth-Heinemann, Burlington, CA.

Berman, J. W. and Bruneau, M. (2009). "Cyclic testing of a buckling restrained braced frame with unconstrained gusset connections." *J. Struct. Eng.*, Vol. 135, No. 12, pp. 1499-1510, DOI: 10.1061/(ASCE)ST.1943-541X.0000078.

Black, C. J., Makris, N., and Aiken, I. D. (2004). "Component testing, seismic evaluation and characterization of buckling restrained braces." *J. Struct. Eng.*, Vol. 130, No. 6, pp. 880-894, DOI: 10.1061/(ASCE)0733-9445(2004)130:6(880).

Celik, O. C. and Bruneau, M. (2007). *Seismic behavior of bidirectional-resistant ductile end diaphragms with unbonded braces in straight or skewed steel bridges*, Rep. MCEER-07-0003, Multidisciplinary Center for Earthquake Engineering Research, Buffalo, NY, USA.

Celik, O. C. and Bruneau, M. (2009). "Seismic behavior of bidirectional-resistant ductile end diaphragms with buckling restrained braces in straight steel bridges." *Eng. Struct.*,Vol. 31, No. 2, pp. 380-393, DOI: 10.1016/j.engstruct.2008.08.013.

Celik, O. C. and Bruneau, M. (2011). "Skewed slab-on-girder steel bridge superstructures with bidirectional ductile end diaphragms."*J. Bridge Eng.*, Vol. 16, No. 2, pp. 207-218, DOI: 10.1061/(ASCE)BE.1943-5592.0000141.

Chen, Q., Wang, C. L., Meng, S., and Zeng, B. (2016). "Effect of the unbonding materials on the mechanic behavior of all-steel buckling restrained braces." *Eng. Struct.,* Vol. 111, pp. 478-493, DOI: 10.1016/j.engstruct.2015.12.030.

Chou, C. C. and Chen, S. Y. (2010). "Subassemblage tests and finite element analyses of sandwiched buckling-restrained braces." *Eng. Struct.*, Vol. 32, pp. 2108-2121, DOI: 10.1016/j.engstruct.2010.03.014.

CimatronE (2012). *Cimatron group, cimatron regional distrubutor*, TEKYAZ Software for Machinery, Istanbul, Turkey.

Fahnestock, L. A., Sause, R., and Ricles, J. M. (2007). "Seismic response and performance of buckling-restrained braced frames." *J. Struct. Eng.*, Vol. 133, No. 9, pp. 1195-1204, DOI: 10.1061/(ASCE)0733-9445(2007)133:9(1195).

Haydaroglu, C. and Celik, O. C. (2012). "Experimental investigation of partially CFRP wrapped steel HSS braces for seismic performance improvement." *15th World Conference on Earthquake Engineering*, Lisbon, Portugal.

Hollomon, J. H. (1945). "Tensile deformation." *Transactions of the Metallurgical Society of AIME*, Vol. 162, pp. 268-290.

Hoveidae, N. and Rafezy, B. (2015). "Local buckling behavior of core plate in all-steel buckling restrained braces." *Int. J. Steel Struct.*, Vol. 15, No. 2, pp. 249-260, DOI: 10.1007/s13296-015-6001-x.

Merritt, S., Uang, C. M., and Benzoni, G. (2003). *Subassemblage testing of star seismic buckling-restrained braces*, Rep. TR-2003/04, Dept.

University of California, La Jolla, CA, USA.

Ragni, L., Zona, A., and Dall'Asta, A. (2011). "Analytical expressions for preliminary design of dissipative bracing systems in steel frames." *J. Constr. Steel Res.*, Vol. 67, No. 1, pp. 102-113, DOI: 10.1016/j.jcsr.2010.07.006.

Sabelli, R., Mahin, S., and Chang, C. (2003). "Seismic demands on steel braced frame buildings with buckling-restrained braces." *Eng. Struct.*, Vol. 25, No. 5, pp. 655-666, DOI: 10.1016/S0141-0296(02)00175-X.

Sutcu, F., Takeuchi, T., and Matsui, R. (2014). "Seismic retrofit design method for RC buildings using buckling-restrained braces and steel frames." *J. Constr. Steel Res.*, Vol. 101, No. 10, pp. 304-313, DOI: 10.1016/j.jcsr.2014.05.023.

Tabatabaei, S. A. R., Mirghaderi, S. R., and Hosseini, A. (2014). "Experimental and numerical developing of reduced length buckling-restrained braces." *Eng. Struct.*, Vol. 77, pp. 143-160, DOI: 10.1016/j.engstruct.2014.07.034.

Takeuchi, T., Hajjar, J. F., Matsui, R., Nishimoto, K., and Aiken, I. D. (2010). "Local buckling restraint condition for core plates in buckling restrained braces." *J. Constr. Steel Res.*, Vol. 66, No. 2, pp. 139-149, DOI: 10.1016/j.jcsr.2009.09.002.

Takeuchi, T., Hajjar, J. F., Matsui, R., Nishimoto, K., and Aiken, I. D. (2012). "Effect of local buckling core plate restraint in buckling restrained braces." *Eng. Struct.*, Vol. 44, pp. 304-311, DOI: 10.1016/j.engstruct.2012.05.026.

Takeuchi, T. and Wada, A. (2017). *Buckling-restrained braces and applications*, The Japan Society of Seismic Isolation (JSSI), Tokyo, Japan.

Tremblay, R., Lacerte, M., and Christopoulos, C. (2008). "Seismic response of multistory buildings with self-centering energy dissipative steel braces." *J. Struct. Eng.*, Vol. 134, No. 1, pp. 108-120, DOI: 10.1061/(ASCE)0733-9445(2008)134:1(108).

Usami, T., Wang, C. L., and Funayama, J. (2012). "Developing high-performance aluminum alloy buckling restrained braces based on series of low-cycle fatigue tests." *Earth. Eng. Struct. Dyn.,* Vol. 41, No. 4, pp. 643-661, DOI: 10.1002/eqe.1149.

Wang, C. L., Usami, T., and Funayama, J. (2012). "Evaluating the influence of stoppers on the low-cycle fatigue properties of high-performance buckling-restrained braces." *Eng. Struct.*, Vol. 41, pp. 167-176, DOI: 10.1016/j.engstruct.2012.03.040.

Wu, B., Lu, J., Mei, Y., and Zhang, J. (2017). "Buckling mechanism and global stability design method of buckling-restrained braces." *J Constr. Steel Res.*, Vol. 138, pp. 473-487, DOI: 10.1016/j.jcsr.2017.07.023.

Zona, A. and Dall'Asta, A. (2012). "Elastoplastic model for steel buckling-restrained braces." *J. Constr. Steel Res.*, Vol. 68, pp. 118-125, DOI: 10.1016/j.jcsr.2011.07.017.